Article

Effects of dynein inhibitor on the number of motor proteins transporting synaptic cargos

Kumiko Hayashi,[1,*] Miki G. Miyamoto,[1] and Shinsuke Niwa[2]
[1]Department of Applied Physics, Graduate School of Engineering and [2]Frontier Research Institute for Interdisciplinary Sciences and Graduate School of Life Science, Tohoku University, Sendai, Japan

ABSTRACT Synaptic cargo transport by kinesin and dynein in hippocampal neurons was investigated by noninvasively measuring the transport force based on nonequilibrium statistical mechanics. Although direct physical measurements such as force measurement using optical tweezers are difficult in an intracellular environment, the noninvasive estimations enabled enumerating force-producing units (FPUs) carrying a cargo comprising the motor proteins generating force. The number of FPUs served as a barometer for stable and long-distance transport by multiple motors, which was then used to quantify the extent of damage to axonal transport by dynarrestin, a dynein inhibitor. We found that dynarrestin decreased the FPU for retrograde transport more than for anterograde transport. This result indicates the applicability of the noninvasive force measurements. In the future, these measurements may be used to quantify damage to axonal transport resulting from neuronal diseases, including Alzheimer's, Parkinson's, and Huntington's diseases.

SIGNIFICANCE Kinesin and dynein transport biomaterial as cargos along microtubules throughout eukaryotic cells. The in vivo mechanisms such as force-velocity curves of cargo transport remain unclear because measuring force in vivo is challenging. In this study, we applied a noninvasive force measurement method to synaptic cargo transport in mouse hippocampal neurons. We identified six force-producing units (FPUs) carrying a cargo comprising the motor proteins generating force for anterograde and retrograde transport. We further found that retrograde FPUs were decreased more than anterograde FPUs in the presence of the dynein inhibitor dynarrestin. These results indicate the applicability of the noninvasive force measurements.

INTRODUCTION

Kinesin and dynein transport biomaterial, packaged in membrane-bound vesicles as "cargo," along microtubules throughout eukaryotic cells (1–3). These motor proteins produce their driving force by hydrolyzing ATP. Physical measurements of this movement, such as force-velocity curves, have been studied in single-molecule experiments (4–9); however, in vivo mechanisms are still unclear because measuring force in vivo is challenging. Stokes' law can be used to estimate in vivo driving force from the velocity v of moving cargo as the drag force through the relationship $F = 6\pi\eta rv$, but cargo viscosity η and the size r are difficult to measure in an intracellular environment. Optical tweezers have been used to measure force exerted

on lipid droplets in cells (10–12), but their application to submicron cargo is limited.

The in vivo driving force produced by motor proteins acting on intracellular cargo was recently investigated through noninvasive force measurements based on nonequilibrium statistical mechanics (13–17). Using the reported method, by inferring the driving force from the fluctuating motion of transported cargo, the number of force-producing units (FPUs) compromising motor proteins carrying a single cargo was estimated as one to three anterograde FPUs for synaptic vesicle precursor transport in motor neurons of *Caenorhabditis elegans* (13), one to four anterograde and one to three retrograde FPUs for endosome transport in mice dorsal ganglion neurons (14), and one to five retrograde FPUs for melanosome transport in zebrafish melanophores. Such multiple motor transport of cargos has been observed in force measurement experiments using optical tweezers (10,11,18), biochemical measurements (19), and analyses of transport velocity (20–23), and is essential for understanding in vivo transport mechanisms.

Because multimotor cooperativity contributes to the stable and long-distance transport of materials along axons to maintain neuronal activity, the number of FPUs hauling a cargo may be a reasonable indicator of healthy neuronal activity. There are many dysfunctions in cargo transport with which abnormal changes of the number of motors is accompanied. For example, mislocation of synapses in a motor neuron of *Caenorhabditis elegans* worms caused by a lack of the accessory protein ARL-8 for synaptic vesicle precursors transport (24) was related to a decreased number of active kinesin motors transporting the cargo vesicles (13). The lack of adaptor proteins interacting with cargo and motors also weakened amyloid precursor protein transport, resulting in a decreased transport velocity (25). Furthermore, the number of motors is strictly regulated in healthy neurons; misregulation of motors in human neurons leads to neuronal diseases. Such an example is the overtransport of synaptic materials by mutant kinesins, which causes hereditary spastic paralysis; the autoinhibition mechanism of the mutant kinesin was dysfunctional, resulting in an increase in active kinesin (26). The excessive transport of dynein-dependent retrograde transport caused by mutations in BICD2, an adaptor for dynein-cargo interaction, is also known to result in spinal muscular atrophy (27). Additionally, the number of motors may be important in mitochondrial arrest regarding the mitophagy of damaged mitochondria by releasing kinesin motors via the adaptor proteins Parkin and PINK1 (28). As numerous dysfunctions can occur when the number of motors transporting cargos is altered, the noninvasive force measurement method enumerating the number of motors can lead to a qualitative understanding of dysfunction of in vivo cargo transport resulting from neuronal diseases. Thus, applications of the noninvasive force measurement are considered to be significant.

In this study, we applied the noninvasive force measurement method to synaptic cargo transport in mouse hippocampal neurons. This study is the first application of the method to cargo transport in mammalian hippocampal neurons. Synaptic proteins are produced and packed in cargo vesicles in the cell body of neurons, after which the cargo vesicles are transported in an anterograde manner to the axon terminus by KIF1A and KIF1Bβ, which are members of the kinesin-3 family, and in a retrograde manner by cytoplasmic dynein in mammalian neurons (1). Particularly, we investigated the number of FPUs carrying synaptic cargos to determine the extent of damage caused by treatment with dynarrestin, a specific small-molecule antagonist of cytoplasmic dynein (29). Artificially controlling the number of motors by using the drug is a useful simulation experiment for investigating dysfunctions in cargo transport. The results obtained from noninvasive force measurements showed that retrograde FPUs were decreased more than anterograde FPUs in the presence of dynarrestin, as expected. The effectiveness of the noninvasive force measurement was demonstrated. Considering the difficulties associated with direct physical measurements in live nonequilibrium neurons, we anticipate that noninvasive force measurement will aid in the determination of physical aspects of synaptic cargo transport mechanisms.

MATERIALS AND METHODS

Primary culture of neurons and transfection

Primary culture of hippocampal neurons was performed as previously described with some modifications (25,30). The hippocampus of wild-type C57BL/6 mice (Japan SLC, Hamamatsu, Japan) at embryonic day 17 was dissected, and neurons were cultured in glass-bottom dishes (Mat-Tek, Ashland, MA) in culture medium (NbActiv4; BrainBits, Springfield, MA), as described previously (25). After culture for 4–7 days, the neurons were transfected with the plasmid vector for green-fluorescence-protein-fused synaptotagmin (31) using the calcium phosphate method (Takara Bio, Shiga, Japan). All animal experiments complied with a protocol approved by the Institutional Animal Care and Use Committee, Tohoku University (2016EgA-003, 2019EgA-001).

Dynarrestin treatment and fluorescence microscopy

Dynarrestin (Tocris Bioscience, Bristol, UK) was added to a culture dish containing neurons at 1 day posttransfection (final concentration of dynarrestin was 100 or 200 μM), and the dish was incubated for 30 min before fluorescence observation and then washed with Hank balanced salt solution (Thermo Fisher Scientific, Waltham, MA) containing 100 or 200 μM dynarrestin.

Cargo movement was observed with a fluorescence microscope (IX83; Olympus, Tokyo, Japan) equipped with a heating plate (CU-201; Live Cell Instrument, Seoul, Korea) maintained at 37°C for 45 min. For this observation, B27-supplement (Thermo Fisher Scientific) and 150 μM 2-mercaptoethanol (Wako Chemical Company, Osaka, Japan) were added to the medium. Images were obtained with a 150× objective lens (UApoN 150×/1.45; Olympus) and an sCMOS camera (OLCA-Flash4.0 v.2.0; Hamamatsu Photonics, Hamamatsu, Japan) at 100 frames/s. The center position of each cargo vesicle was determined from the recorded images using custom software written in LabVIEW 2013 (National Instruments, Austin, TX), as described previously (13).

The primary culture of neurons was repeated 10 times, and data were collected from six to eight preparations for each dynarrestin concentration. To examine anterograde and retrograde transport, we investigated 131 and 116 cargos from 50 to 39 different cells, respectively, for untreated cells; 92 and 102 cargos from 35 to 37 different cells, respectively, treated with 100 μM dynarrestin; and 119 and 123 cargos from 43 to 41 different cells, respectively, treated with 200 μM dynarrestin. Additionally, from six preparations, we investigated 122 and 127 cargos from 25 to 27 different cells, respectively, for anterograde and retrograde transport at a recording rate of 200 frames/s (Fig. S1); from four preparations, we investigated 40 and 74 cargos from 19 to 26 different cells, respectively, treated with 50 μM dynarrestin (Fig. S2). The cells used for observation were chosen randomly after visual inspection.

The precision of the positional measurements was verified with beads (300-nm latex beads; Polyscience, Niles, IL) that were similar in size to the synaptic cargos. The standard deviation of the bead position tightly attached to the glass surface was 8.3 ± 1.2 nm ($n = 4$ different beads).

Calculation of χ

The force index χ introduced in our previous studies (13–15) was originally defined using the idea of the fluctuation theorem as follows:
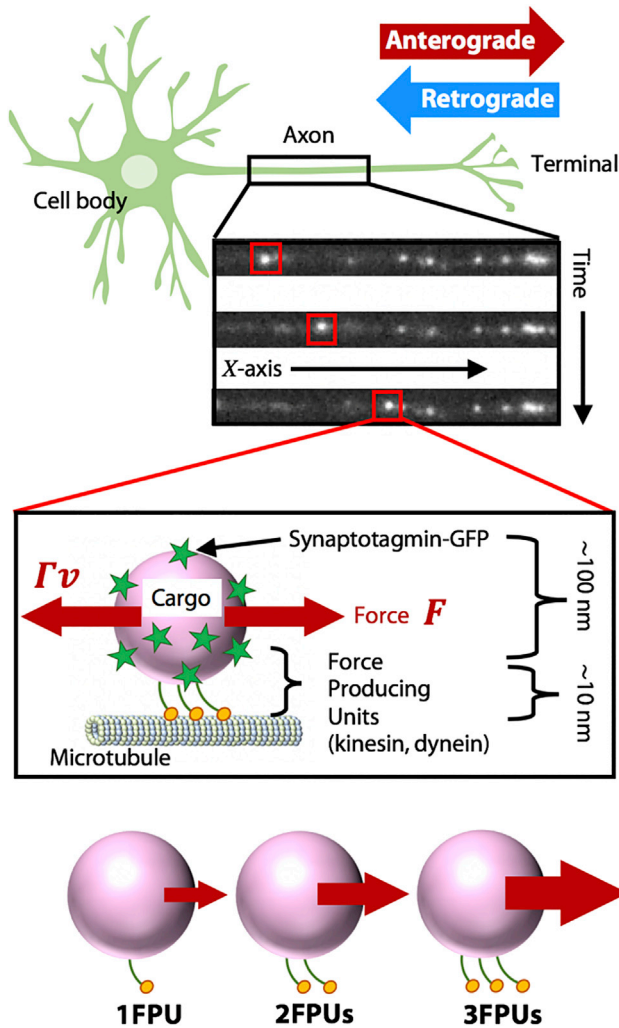
FIGURE 1 Synaptic cargo transport in the axon of a hippocampal neuron. Synaptic cargos (*pink circles*) labeled with GFP (*green stars*) undergo anterograde transport by kinesin and retrograde transport by dynein along microtubules (*green cylinder*). White dots in the fluorescence micrographs represent synaptic cargo. The force (F) is generated by the motor proteins and equivalent to the drag force, Γv, at a CVS, where v and Γ represent the velocity and friction coefficient of moving cargo, respectively. A single cargo transported by multiple FPUs is shown(*bottom*). To see this figure in color, go online.

$$\chi = \ln[P(\Delta X) / P(-\Delta X)]/\Delta X, \qquad (1)$$

from the distribution $P(\Delta X)$ of the displacement $\Delta X = X(t+\Delta t) - X(t)$ (Fig. 2 B). $P(\Delta X)$ was fitted to a Gaussian function (Fig. 2 C):

$$P(\Delta X) = \exp\left(-\left(\Delta X - b\right)^2 / 2a\right)/(2\pi a)^{0.5}, \qquad (2)$$

where the fitting parameters a and b correspond to the variance and mean of the distribution, respectively. By inserting Eq. 2 into Eq. 1, we obtain:

$$\chi = 2b/a \qquad (3)$$

Equation 3 is equivalent to the equation $\chi = v/D$ when the diffusion coefficient D is defined as $D = a/2\Delta t$. The error of χ was estimated at 10%

based on the bootstrapping method (13,15), and χ calculated from different partial segments (n = 10) cut from the original constant velocity segments (CVS) is depicted in Fig. 2 A, whose length was 50% of the original segment (Fig. 2 D, *thin curves*). CVS were chosen so that ΔX calculated from the CVS belonged to the same statistics population (Fig. S3).

A smoothing filter was applied to the values of χ to reduce variation in the raw data for χ as a function of Δt. We used the following simple averaging filter:

$$\chi^{\mathrm{f}}(\Delta t) = (\chi(\Delta t-10 \text{ ms}) + \chi(\Delta t) + \chi(\Delta t + 10 \text{ ms}))/3 \quad (4)$$

Note that $\chi^{\mathrm{f}}(\Delta t) = (\chi(\Delta t) + \chi(\Delta t + 10 \text{ ms}))/2$ for $\Delta t = 10$ ms and $\chi^{\mathrm{f}}(\Delta t) = (\chi(\Delta t - 10 \text{ ms}) + \chi(\Delta t))/2$ for $\Delta t = 150$ ms. The software used to calculate χ is available from a website (https://github.com/kumikohayashia2/mmc).

Classification of χ-Δt plots

Affinity propagation (32,33), an exemplar-based clustering method that does not require the number of clusters, was adopted to cluster the two-dimensional data ($\sqrt{\chi^{\mathrm{f}}(\Delta t = 130 \text{ ms})}$, $\sqrt{\chi^{\mathrm{f}}(\Delta t = 150 \text{ ms})}$). The square root of χ was used to apply the cluster method to make the distance between adjoining clusters constant, because the value of χ was observed to exponentially increase as the number of FPUs increased, although the reason for this is unclear. Two-dimensional data($\chi^{\mathrm{f}}(\Delta t = 130 \text{ ms})$, $\chi^{\mathrm{f}}(\Delta t = 150 \text{ ms})$) were also available for the clustering, although these data were less stable (retrograde χ was decreased in the presence of dynarrestin (Fig. 6 B), making clustering analysis difficult).

The clustering method was applied using the "APCluster" package in R (34). Clustering was stable for the wide range of values for the sole parameter (q) of affinity propagation analysis. Because the result of clustering may depend on the sample size, the stability of the cluster number against the sample sizes was checked in a bootstrapping manner; cluster analysis was performed 20 times for half of the samples which were chosen randomly among the original samples (see Fig. S4).

Statistical test

Students t-test was applied by using the function (t.test()) in R software (34) to the data in Fig. 5, *B–C* and 6. The p-values are as follows: **$p < 0.01$ and ***$p < 0.001$.

RESULTS

Fluctuation of CVSs of moving cargo

The motion of synaptic cargo, including synaptotagmin labeled with (GFP) (31), along the axon of mouse hippocampal neurons was observed by fluorescence microscopy (Fig. 1). Although the axons were crowded with cargos, we were able to track a few individually. The center position (X) of each cargo was obtained from fluorescence images (Materials and methods). Fig. 2 A shows a typical example time course of the cargo position (see Fig. S5 A and S6 A for other examples). We observed that cargo velocities changed over the course of several seconds. Particularly, the CVSs of the time courses (Fig. 2 A, *square*) with velocities greater than 100 nm/s and lasting for more than 0.5 s were used for the following analyses on driving force (Fig. 1), assuming that the CVS fluctuation (Fig. 2 B) in one direction
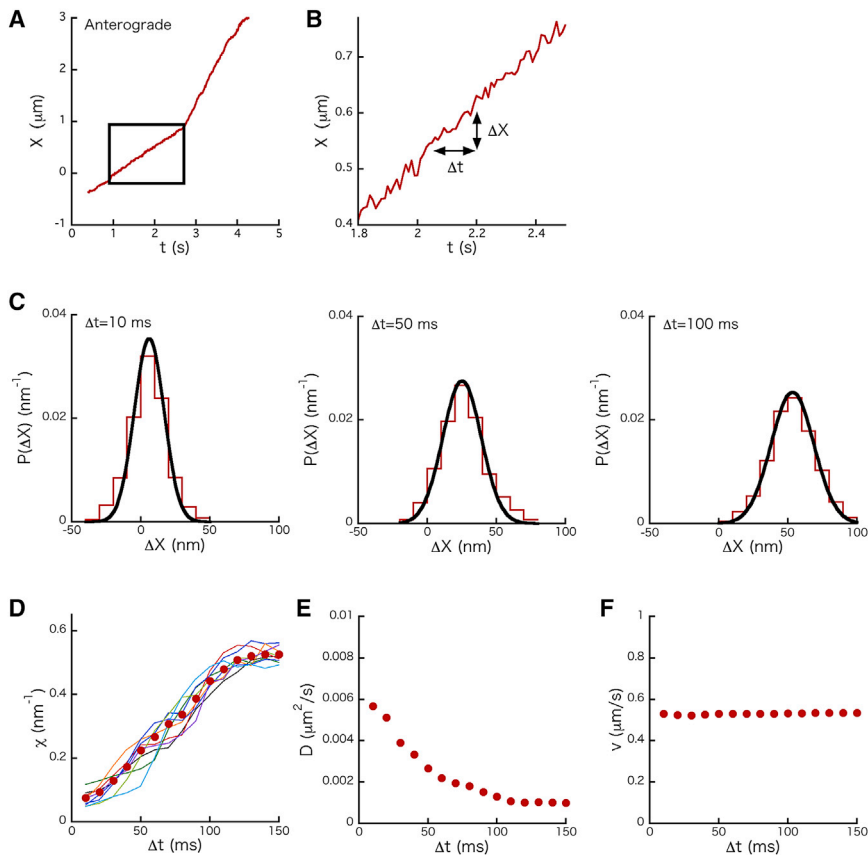
FIGURE 2 Fluctuation of position of a transported cargo. (*A*) Typical example of cargo position (*X*) over time. The boxed time interval is aCVS. (*B*) Magnified view of the time course (Fig. 2 *A*) at a CVS. $\Delta X = X(t + \Delta t) - X(t)$. (*C*) Distribution $P(\Delta X)$ of ΔX for the cases in which $\Delta t = 10$ ms (*left*), 50 ms (*middle*), and 100 ms (*right*). $P(\Delta X)$ fit a Gaussian distribution (*black curve*). (*D*) Example of χ ($n = 1$) for the CVS (Fig. 2 *A*) calculated using Eq. 3 plotted as a function of Δt (the *thick curve*). The thin curves represent χ calculated from different partial segments cut from the original CVS to estimate the error of χ in a bootstrapping manner (Materials and methods). After relaxation time (~100 ms), χ reached a constant value. (*E* and *F*) Noting that $\chi = v/D$ (Eq. 3), where D and v are the diffusion coefficient and velocity of a cargo, respectively, Δt dependence of D and v were also shown. To see this figure in color, go online.

was affected minimally by other motors (the assumption is discussed in the Conclusion and discussion).

The fluctuation of a CVS is represented by the distribution $P(\Delta X)$, where $\Delta X = X(t + \Delta t) - X(t)$ (Fig. 2 *B*). $P(\Delta X)$ is plotted when $\Delta t = 10$, 50, and 100 ms (Fig. 2 *C*). The peak of $P(\Delta X)$ shifts to the right because of the directional motion of transported cargo, and variance increases because of the diffusional effect as Δt becomes larger. $P(\Delta X)$ was well-described by a Gaussian function similar to those measured for other intracellular cargos (13–15). Note that the abnormal diffusion property (i.e., $P(\Delta X)$ is not a Gaussian function) often reported for intercellular cargo transport (35–38) appeared upon analysis of the whole trajectory without dividing it into CVSs (39). One reason for this abnormality may be that the trajectory includes multiple velocity values.

Force index (χ) and quantification of FPUs transporting a cargo

Using $P(\Delta X)$ calculated in Fig. 2 *C*, an example force index χ (Eq. 3) for the CVS was calculated as a function of Δt as described in Materials and methods (Fig. 2 *D*, *thick curve*). Over time, the index converged to a constant value ($\Delta t > 100$ ms). Noting that χ can be rewritten as v/D (Eq. 3), the relaxation time was found to result from that of D (Fig. 2

E) rather than that of v (Fig. 2 *F*), which is characteristic for microscopic interactions, such as tethering interactions between cargo and microtubules, collisions with other organelles and cytoskeletons, and ATP hydrolysis by motors (14). Such Δt-dependence of D caused by microscopic interactions was studied theoretically (40). Whereas D for a small Δt was considered to be dominated by microscopic interactions and experimental noise, D for a large Δt was considered to represent a fluctuating property of synaptic cargos because D was negatively correlated with their sizes ($r = -0.47$), whose size dependence was similar to that of v (Fig. S7). On the other hand, D was not strongly dependent on motors because it was almost constant when the number of motors was changed (Fig. S8).

Next, we plotted χ for ~100 anterograde (Fig. 3 *A*, *left*)- and retrograde (Fig. 4 *A*, *left*)-moving cargos. Note that the direction in motion was set as positive when χ was calculated. The discreteness of χ was found with synaptic cargo transport and was observed previously for other cargo transports (13–15). After applying a classification method, we found six clusters for both anterograde (Fig. 3 *A*) and retrograde (Fig. 4 *A*) transport. This indicates that we identified six FPUs when the discreteness of the force index χ represented the discreteness of the transport force. Note that two trajectories of χ (~2 nm^{-1}) were excluded from cluster analysis for retrograde transport because this analysis became difficult when a small
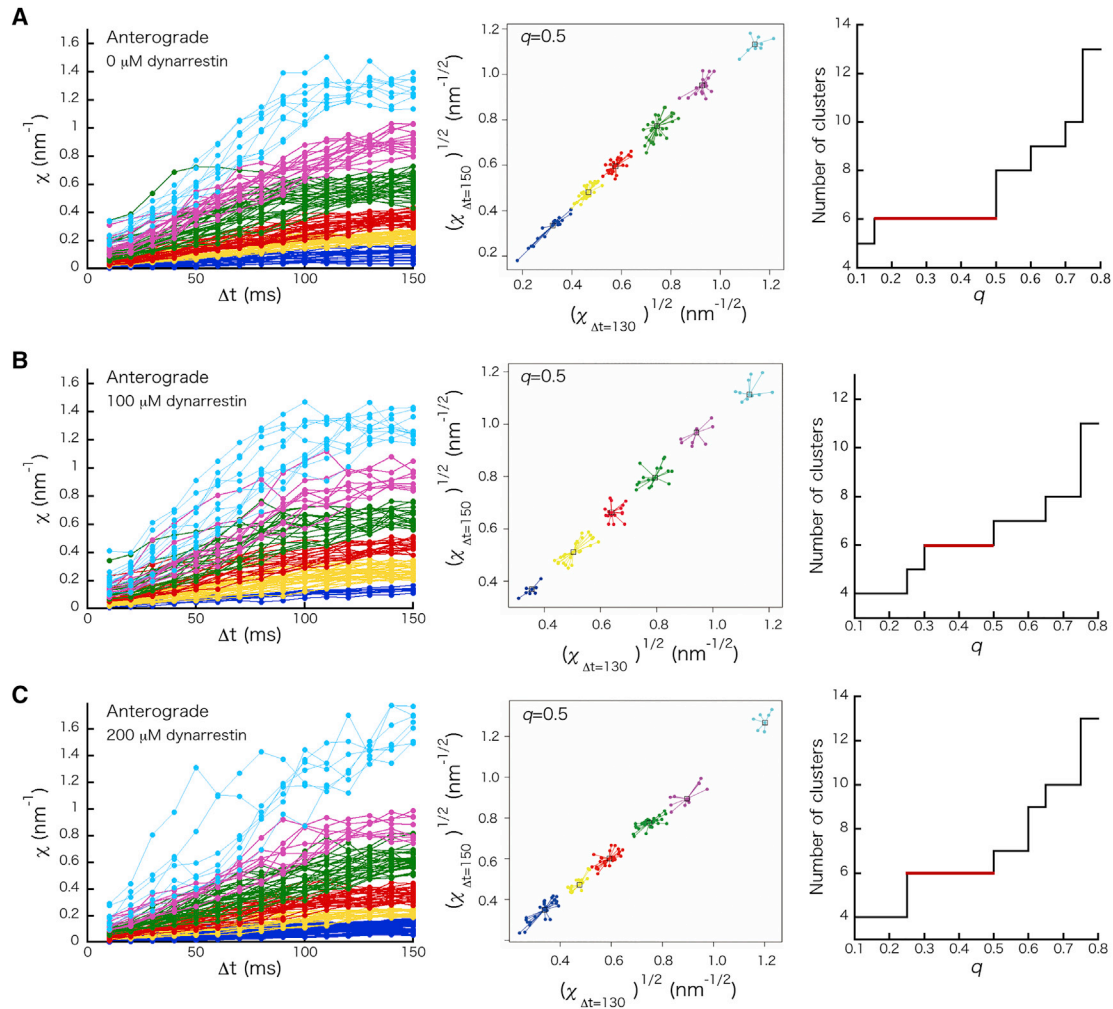
FIGURE 3   Force index χ for anterograde transport. Shown here is χ as a function of Δt for n different cargos in cells treated with (A) 0 μM dynarrestin ($n = 131$), (B) 100 μM dynarrestin ($n = 92$), and (C) 200 μM dynarrestin ($n = 119$) (left panels). Each color denotes a cluster (i.e., FPU). The number of clusters was determined by clustering analysis (described in Materials and methods) (middle panels). The number of clusters are displayed as a function of q, which is the sole parameter of the cluster analysis (right panels). The most probable cluster number was decided as the number valid for the wide range of q. To see this figure in color, go online.

number of trajectories of χ were included (see Fig. S9 for the trajectories). The stability of six clusters against sample sizes was checked using a bootstrapping method (Fig. S4). In addition, six clusters were observed when we recorded at a rate of 200 frames/s (Fig. S1), indicating that the results did not strongly depend on the recording rate.

One candidate FPU is thought to be composed of a kinesin dimer for anterograde transport, and four monomers of dynein have been implicated for retrograde transport according to cryoelectron microscopy analysis (41). However, the constitution of one FPU has not been determined, as described in the Conclusion and discussion.

Addition of dynein inhibitor

We investigated the effect of the drug dynarrestin on synaptic cargo transport to determine whether χ can detect the

motor number change caused by the inhibitor. Dynarrestin inhibits ATPase activity of members of the AAA + ATPase superfamily, including dynein (29). We treated neurons with 100 and 200 μM dynarrestin and plotted anterograde (Fig. 3, B and C) and retrograde (Fig. 4, B and C) transport. Although the changes in anterograde FPUs were small, the fraction of cargos with one FPU increased in the presence of 200 μM dynarrestin (Fig. 5 A, black arrow), and retrograde FPUs showed larger decreases following dynarrestin treatment (Fig. 5 B).

Compared with the large decrease in the number of retrograde FPUs (Fig. 5 B), the decrease in velocity (v) in the presence of dynarrestin was small (Fig. 5 C). As v depends on the cargo size (Fig. S7, right) and number of FPUs, this small change in velocity is explained by the relationship between χ and v (Fig. 5 D). Cargo with large FPUs did not always move with the greatest velocity because the
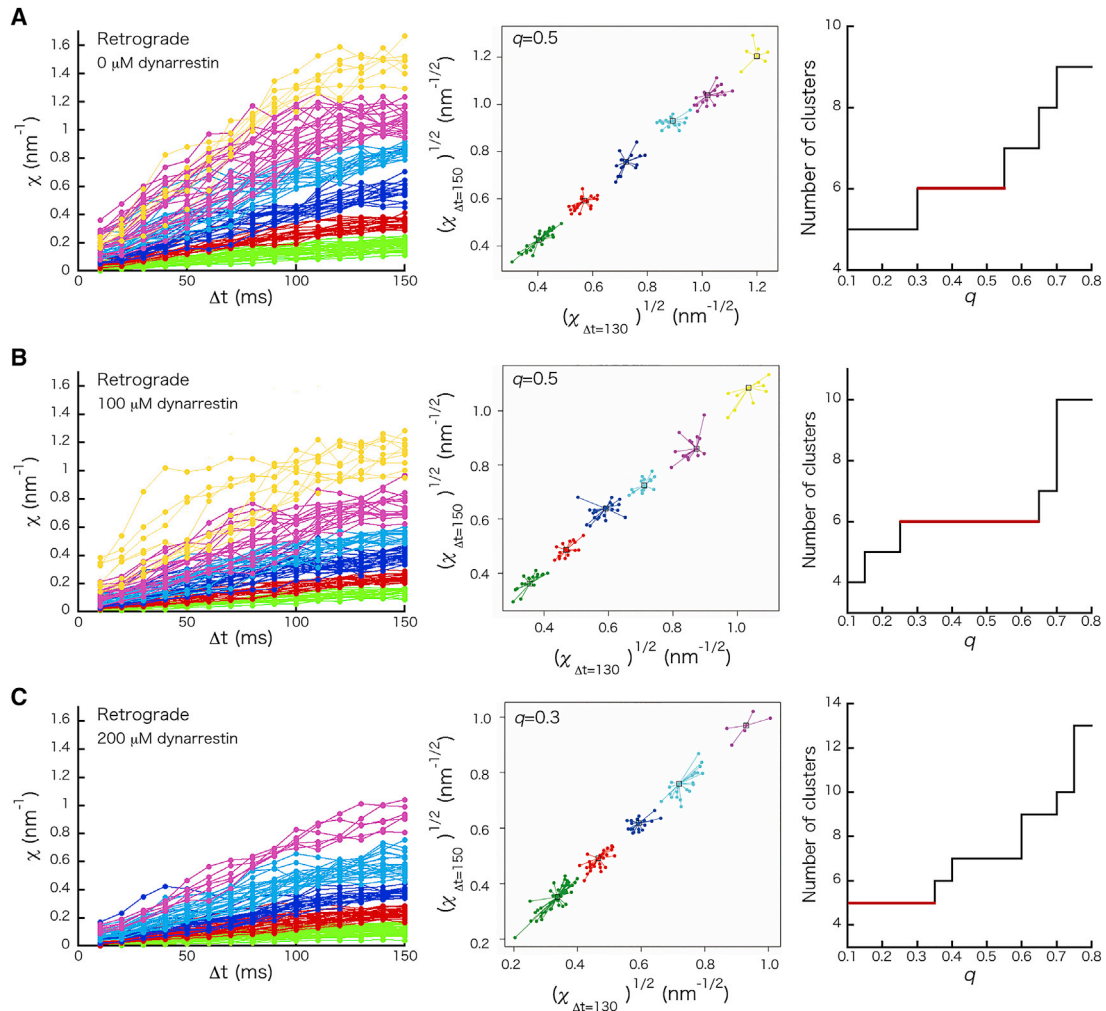
FIGURE 4 Force index χ for retrograde transport. Shown here is χ as a function of Δt for n different cargos in cells treated with (*A*) 0 μM dynarrestin ($n = 116$), (*B*) 100 μM dynarrestin ($n = 102$), and (*C*) 200 μM dynarrestin ($n = 123$) (*left panels*). Each color denotes a cluster (i.e., FPU). The number of clusters was decided by clustering analysis (described in Materials and methods) (*middle panels*). The right panels show the number of clusters as a function of q, which is the sole parameter of the cluster analysis. The most probable cluster number was decided as the number valid for the wide range of q. To see this figure in color, go online.

fluorescence intensities of cargo, which represent the sizes of cargos, with six FPUs were greater than for other cargos (Fig. 5 *E*). This indicates that the lack of large FPUs caused by dynarrestin treatment only slightly decreased the velocity.

The trajectories of χ for each FPU were compared among different dynarrestin concentrations in terms of anterograde (Fig. 6 *A*) and retrograde (Fig. 6 *B*) transport. A systematic decrease in χ was observed only for retrograde transport, whereas anterograde transport only slightly changed upon dynarrestin treatment. This trend may have resulted from damage caused by the inhibitors to some multiple dynein monomers constituting one retrograde FPU. Then, to investigate the constitution of one retrograde FPU, we plotted the convergent values of χ, regarded as $\chi(\Delta t = 150\text{ms})$, as a function of the dynarrestin concentration (Fig. 7). The quantity converged and decreased by approximately half as the

concentration became large. This indicates that one retrograde FPU may comprise multiple monomers of dynein, and that the minimal unit to generate force may be a half of one FPU. Further studies are needed to resolve this important question.

DISCUSSION

We performed fluorescence microscopy to observe synaptic cargo in the axons of mouse hippocampal neurons, in which cargo undergo anterograde transport by KIF1A and KIF1β and retrograde transport by cytoplasmic dynein (Fig. 1). Given that cooperative activity by multiple motors contributes to stable and long-distance transport, and that FPU number represents an index of healthy axonal transport, we measured the force index χ (Eq. 3) and identified six FPUs used for anterograde (Fig. 3 *A*) and retrograde
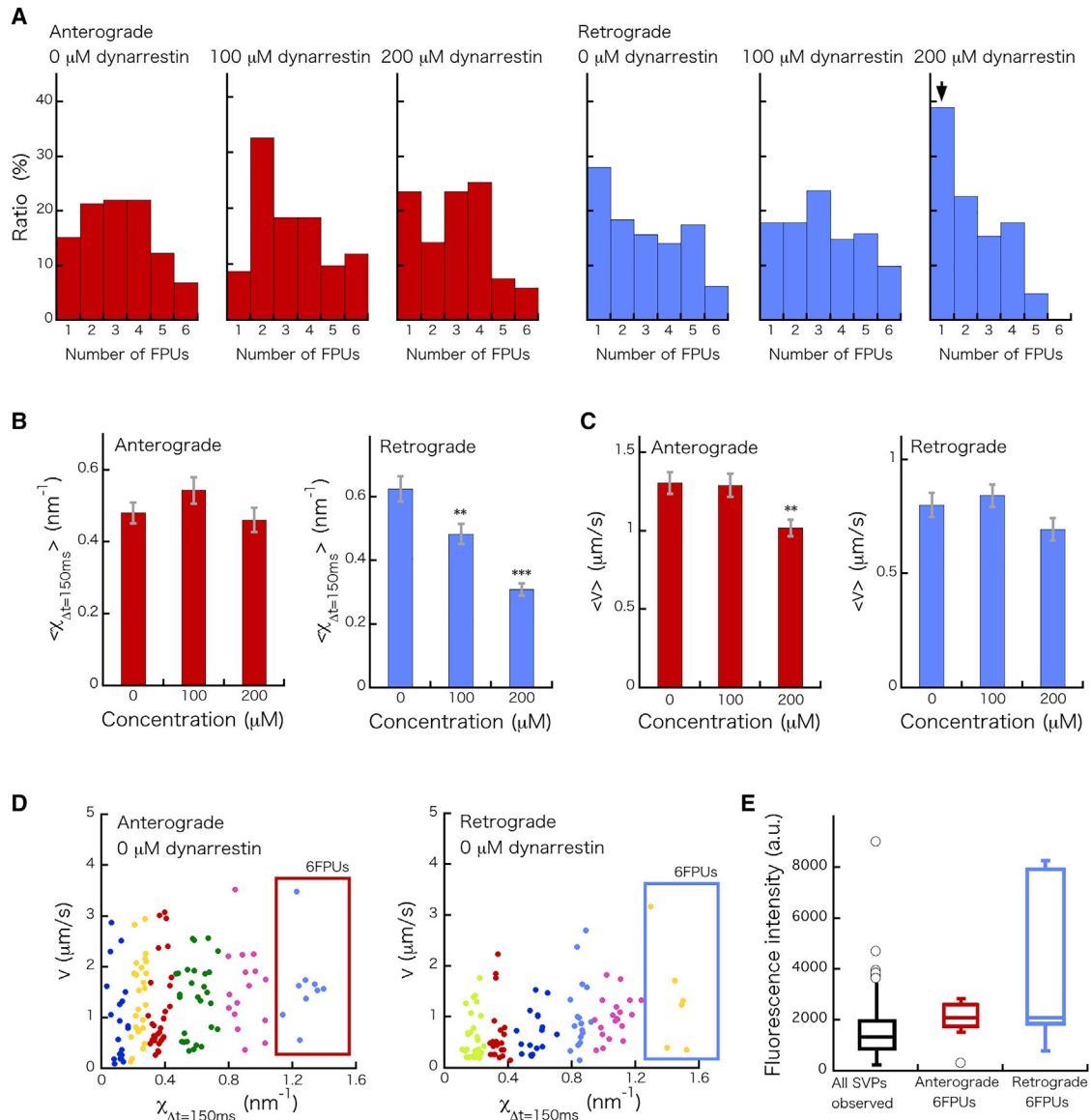
FIGURE 5 Relationship between χ, velocity, and fluorescence intensity. (A) Number of the elements for each FPU, calculated from the results in Fig. 3 and 4, representing as probability density. (B) Mean values of χ as a function of dynarrestin concentration for anterograde (*left*) and retrograde (*right*) transport. Error bars represent standard error (SE). (C) Mean velocity (*v*) at the CVSs as a function of dynarrestin concentration for anterograde (*left*) and retrograde (*right*) transport. Error bars represent SE. (D) Relationship between χ in the case $\Delta t = 150$ ms and *v* in the absence of dynarrestin for the case of anterograde (*left*) and retrograde (*right*) transport. Each color of the dots denotes each cluster shown in Fig. 3 *A* and 4 *A*, respectively. (E) Comparison among fluorescence intensities of all cargos observed, anterograde cargos belonging to six FPUs, and retrograde cargos belonging to six FPUs, respectively. To see this figure in color, go online.

(Fig. 4 *A*) transport. We then quantified the effect of the dynein inhibitor dynarrestin (29) on cargo transport (Fig. 5, *A* and *B*). Given the difficulty of direct physical measurement in cells, application of this technique will improve the understanding of the mechanisms of intracellular cargo transport, including the roles of adaptor proteins connecting cargos and motors (25).

Synaptic vesicle precursor transport by UNC-104 kinesin in the motor neuron of *C. elegans* worms was investigated previously by the noninvasive force measurement method, and the maximal number of FPUs hauling an synaptic

vesicle precursor was found to be four (13). We found in present study that the maximal number of FPUs on synaptic vesicle precursor is six in mouse neurons. One possibility is that the number of FPUs is related to the size of cargo vesicles. Consistent with this idea, the size of synaptic vesicle precursors visualized by GFP in mammalian neurons is larger than worm neurons (Fig. S10). Although the standard deviations were estimated to be larger than the actual cargo sizes because of limited spatial resolution, the cargo sizes were likely larger in the case of mammalian neurons. Note that our estimated cargo sizes were similar to those
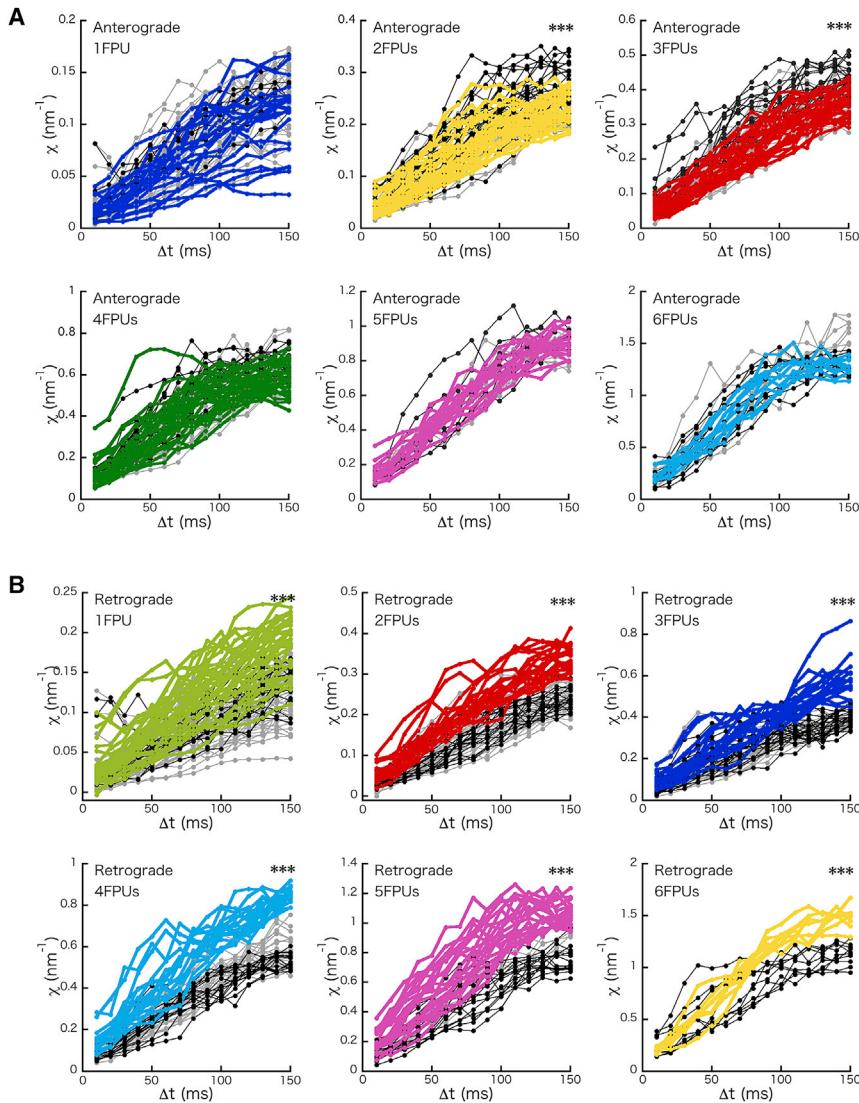
FIGURE 6 The trajectories of χ for each FPU in the cases of anterograde (A) and retrograde (B) transport. The colored, black, and gray trajectories represent the cases of 0, 100, and 200 μM dynarrestin, respectively. The statistical analysis was performed between the sets of χ (Δt=10–150 ms) for the case of 0 μM dynarrestin and those for the case of 100 or 200 μM dynarrestin. To see this figure in color, go online.

previously reported (42). These results suggest that the maximal number of FPUs transporting a single cargo depends on the cargo size, which seemed to be consistent with the results shown in Fig. 5 E that the sizes of cargos for six FPUs were greater than for other cargos.

Next, we consider the assumption that the CVS fluctuation (Fig. 2 B) in one direction was minimally affected by motors that transport or move in the opposite direction. This assumption is not trivial because the tug-of-war motion between two motors (43–46), which could be an origin of this fluctuation, occurs during changes in direction. Because the mean value of the anterograde force index χ for each FPU changed minimally (Fig. 6 A) along with decrease of the retrograde FPUs caused by the inhibitor (Fig. 5 B), this indicated that CVS fluctuation in one direction was not sensitive to the number of other motors. Thus, CVSs were considered separately from tug-of-war segments (44).

Thirdly, the constitution of one retrograde FPU should be discussed. The graph in Fig. 7 shows that the force index χ for one retrograde FPU was convergent and decreased approximately by half as the concentration of dynarrestin increased. This indicates that one retrograde FPU may comprise multiple monomers of dynein, and that the minimal unit to generate force may be a half of one FPU. These conjectures were in accordance with the facts that dynein functions as two dynein dimers based on the observations of cryoelectron microscopy (41) and single-molecule experiment (47).

Finally, the physical aspect of the conversion constant from χ (Eq. 2) to F was discussed. Based on the fluctuation theorem (48,49), the relationship between χ and the driving force (F) is represented as follows,

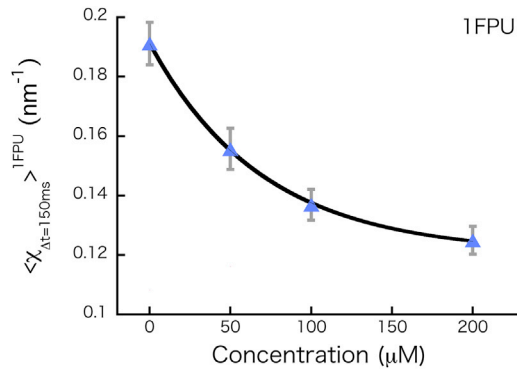$$F = \chi\, k_{\mathrm{B}} T_{\mathrm{eff}}, \qquad (5)$$

FIGURE 7 $\langle \chi_{\Delta t=150\ ms} \rangle$ in the case of one retrograde FPU as a function of dynarrestin concentration. Error bars represent standard error (SE). The black fitting curve represents $0.071 exp(-\ [\text{concentration}]\ /70)+\ 0.12$. The data for 50 µM dynarrestin are shown in Fig. S2. To see this figure in color, go online.

where k_B is the Boltzmann constant and T_{eff} is an effective temperature (14,15), which is a generalized temperature in a nonequilibrium system (40,50,51). In our previous studies on intracellular cargo transport (13–15), T_{eff} was not equal to the temperature of the environment (T) because of nonequilibrium effects. When one anterograde FPU corresponded to a kinesin dimer (which has a stall force of ~5 pN), $k_B T_{eff}$ was estimated to be ~10 times $k_B T$ for synaptic cargo transport. Note that when T_{eff} takes a different value for each moving cargo, the discreteness of the force index χ disappears. Indeed, the constancy of T_{eff} was cross-checked with the relationship $\chi \propto v$ derived from Eq. 1 and the Stokes relationship $F = \Gamma v$ (Γ symbolizing the friction coefficient) for the long time courses of the same cargos, in which Γ of the same cargo was considered constant during the time courses (Fig. S5–S6, S8).

SUPPORTING MATERIAL

Supporting Material can be found online at https://doi.org/10.1016/j.bpj. 2021.02.018.

AUTHOR CONTRIBUTIONS

K.H. and M.G.M. performed the experiments. K.H. analyzed the data and wrote the article with contributions from S.N.

ACKNOWLEDGMENTS

REFERENCES

1. Hirokawa, N., Y. Noda, …, S. Niwa. 2009. Kinesin superfamily motor proteins and intracellular transport. *Nat. Rev. Mol. Cell Biol.* 10:682–696.

2. Vale, R. D. 2003. The molecular motor toolbox for intracellular transport. *Cell.* 112:467–480.

3. Guedes-Dias, P., and E. L. F. Holzbaur. 2019. Axonal transport: driving synaptic function. *Science.* 366:eaaw9997.

4. Nishiyama, M., H. Higuchi, and T. Yanagida. 2002. Chemomechanical coupling of the forward and backward steps of single kinesin molecules. *Nat. Cell Biol.* 4:790–797.

5. Okada, Y., H. Higuchi, and N. Hirokawa. 2003. Processivity of the single-headed kinesin KIF1A through biased binding to tubulin. *Nature.* 424:574–577.

6. Schnitzer, M. J., K. Visscher, and S. M. Block. 2000. Force production by single kinesin motors. *Nat. Cell Biol.* 2:718–723.

7. Tomishige, M., D. R. Klopfenstein, and R. D. Vale. 2002. Conversion of Unc104/KIF1A kinesin into a processive motor after dimerization. *Science.* 297:2263–2267.

8. Vale, R. D., T. Funatsu, …, T. Yanagida. 1996. Direct observation of single kinesin molecules moving along microtubules. *Nature.* 380:451–453.

9. Visscher, K., M. J. Schnitzer, and S. M. Block. 1999. Single kinesin molecules studied with a molecular force clamp. *Nature.* 400:184–189.

10. Shubeita, G. T., S. L. Tran, …, S. P. Gross. 2008. Consequences of motor copy number on the intracellular transport of kinesin-1-driven lipid droplets. *Cell.* 135:1098–1107.

11. Leidel, C., R. A. Longoria, …, G. T. Shubeita. 2012. Measuring molecular motor forces in vivo: implications for tug-of-war models of bidirectional transport. *Biophys. J.* 103:492–500.

12. Jun, Y., S. K. Tripathy, …, S. P. Gross. 2014. Calibration of optical tweezers for in vivo force measurements: how do different approaches compare? *Biophys. J.* 107:1474–1484.

13. Hayashi, K., S. Hasegawa, …, S. Niwa. 2018. Non-invasive force measurement reveals the number of active kinesins on a synaptic vesicle precursor in axonal transport regulated by ARL-8. *Phys. Chem. Chem. Phys.* 20:3403–3410.

14. Hayashi, K., Y. Tsuchizawa, M. Iwaki, and Y. Okada. 2018. Application of the fluctuation theorem for non-invasive force measurement in living neuronal axons. *Mol. Biol. Cell.* 29:3017–3025.

15. Hasegawa, S., T. Sagawa, …, K. Hayashi. 2019. Investigation of multiple-dynein transport of melanosomes by non-invasive force measurement using fluctuation unit χ. *Sci. Rep.* 9:5099.

16. Hayashi, K., S. Matsumoto, …, S. Niwa. 2019. Physical parameters describing neuronal cargo transport by kinesin UNC-104. *Biophys. Rev.* 11:471–482.

17. Hayashi, K. 2018. Application of the fluctuation theorem to motor proteins: from F$_1$-ATPase to axonal cargo transport by kinesin and dynein. *Biophys. Rev.* 10:1311–1321.

18. Rai, A., D. Pathak, …, R. Mallik. 2016. Dynein clusters into lipid microdomains on phagosomes to drive rapid transport toward lysosomes. *Cell.* 164:722–734.

19. Hendricks, A. G., E. Perlson, …, E. L. Holzbaur. 2010. Motor coordination via a tug-of-war mechanism drives bidirectional vesicle transport. *Curr. Biol.* 20:697–702.

20. Shtridelman, Y., T. Cahyuti, …, J. C. Macosko. 2008. Force-velocity curves of motor proteins cooperating in vivo. *Cell Biochem. Biophys.* 52:19–29.

21. Levi, V., A. S. Serpinskaya, …, V. Gelfand. 2006. Organelle transport along microtubules in Xenopus melanophores: evidence for cooperation between multiple motors. *Biophys. J.* 90:318–327.

22. Hill, D. B., M. J. Plaza, …, G. Holzwarth. 2004. Fast vesicle transport in PC12 neurites: velocities and forces. *Eur. Biophys. J.* 33:623–632.

23. Chowdary, P. D., D. L. Che, …, B. Cui. 2015. Nanoparticle-assisted optical tethering of endosomes reveals the cooperative function of dyneins in retrograde axonal transport. *Sci. Rep.* 5:18059.

24. Niwa, S., D. M. Lipton, …, K. Shen. 2016. Autoinhibition of a neuronal kinesin UNC-104/KIF1A regulates the size and density of synapses. *Cell Rep.* 16:2129–2141.

25. Chiba, K., M. Araseki, …, T. Suzuki. 2014. Quantitative analysis of APP axonal transport in neurons: role of JIP1 in enhanced APP anterograde transport. *Mol. Biol. Cell.* 25:3569–3580.

26. Chiba, K., H. Takahashi, …, S. Niwa. 2019. Disease-associated mutations hyperactivate KIF1A motility and anterograde axonal transport of synaptic vesicle precursors. *Proc. Natl. Acad. Sci. USA.* 116:18429–18434.

27. Huynh, W., and R. D. Vale. 2017. Disease-associated mutations in human BICD2 hyperactivate motility of dynein-dynactin. *J. Cell Biol.* 216:3051–3060.

28. Wang, X., D. Winter, …, T. L. Schwarz. 2011. PINK1 and Parkin target Miro for phosphorylation and degradation to arrest mitochondrial motility. *Cell.* 147:893–906.

29. Höing, S., T. Y. Yeh, …, J. Sterneckert. 2018. Dynarrestin, a novel inhibitor of Cytoplasmic dynein. *Cell Chem. Biol.* 25:357–369.e6.

30. Bartlett, W. P., and G. A. Banker. 1984. An electron microscopic study of the development of axons and dendrites by hippocampal neurons in culture. I. Cells which develop without intercellular contacts. *J. Neurosci.* 4:1944–1953.

31. Niwa, S., H. Takahashi, and N. Hirokawa. 2013. β-Tubulin mutations that cause severe neuropathies disrupt axonal transport. *EMBO J.* 32:1352–1364.

32. Frey, B. J., and D. Dueck. 2007. Clustering by passing messages between data points. *Science.* 315:972–976.

33. Bodenhofer, U., A. Kothmeier, and S. Hochreiter. 2011. APCluster: an R package for affinity propagation clustering. *Bioinformatics.* 27:2463–2464.

34. R Core Team.. 2018. R: A language and environment for statistical computing. R Foundation for Statistical Computing.

35. Fakhri, N., A. D. Wessel, …, C. F. Schmidt. 2014. High-resolution mapping of intracellular fluctuations using carbon nanotubes. *Science.* 344:1031–1035.

36. Shin, K., S. Song, …, K. T. Lee. 2019. Anomalous dynamics of in vivo Cargo delivery by motor protein multiplexes. *J. Phys. Chem. Lett.* 10:3071–3079.

37. Posey, D., P. Blaisdell-Pijuan, …, W. W. Ahmed. 2018. Small-scale displacement fluctuations of vesicles in fibroblasts. *Sci. Rep.* 8:13294.

38. Tabei, S. M., S. Burov, …, N. F. Scherer. 2013. Intracellular transport of insulin granules is a subordinated random walk. *Proc. Natl. Acad. Sci. USA.* 110:4911–4916.

39. Hayashi, K., C. G. Pack, …, Y. Okada. 2013. Viscosity and drag force involved in organelle transport: investigation of the fluctuation dissipation theorem. *Eur Phys J E Soft Matter.* 36:136.

40. Hayashi, K., and S. Sasa. 2004. Effective temperature in nonequilibrium steady states of Langevin systems with a tilted periodic potential. *Phys. Rev. E Stat. Nonlin. Soft Matter Phys.* 69:066119.

41. Urnavicius, L., C. K. Lau, …, A. P. Carter. 2018. Cryo-EM shows how dynactin recruits two dyneins for faster movement. *Nature.* 554:202–206.

42. Nakata, T., S. Terada, and N. Hirokawa. 1998. Visualization of the dynamics of synaptic vesicle and plasma membrane proteins in living axons. *J. Cell Biol.* 140:659–674.

43. Gross, S. P. 2004. Hither and yon: a review of bi-directional microtubule-based transport. *Phys. Biol.* 1:R1–R11.

44. Soppina, V., A. K. Rai, …, R. Mallik. 2009. Tug-of-war between dissimilar teams of microtubule motors regulates transport and fission of endosomes. *Proc. Natl. Acad. Sci. USA.* 106:19381–19386.

45. Müller, M. J., S. Klumpp, and R. Lipowsky. 2008. Tug-of-war as a cooperative mechanism for bidirectional cargo transport by molecular motors. *Proc. Natl. Acad. Sci. USA.* 105:4609–4614.

46. Welte, M. A. 2004. Bidirectional transport along microtubules. *Curr. Biol.* 14:R525–R537.

47. Elshenawy, M. M., J. T. Canty, …, A. Yildiz. 2019. Cargo adaptors regulate stepping and force generation of mammalian dynein-dynactin. *Nat. Chem. Biol.* 15:1093–1101.

48. Evans, D. J., E. G. Cohen, and G. P. Morriss. 1993. Probability of second law violations in shearing steady states. *Phys. Rev. Lett.* 71:2401–2404.

49. Ciliberto, S., S. Joubaud, and A. Petrosyan. 2010. Fluctuation in out-of-equilibrium systems: from theory to experiment. *J. Stat. Mech.* 2010:P12003.

50. Cugliandolo, L. F. 2011. The effective temperature. *J. Phys. A Math. Theor.* 44:483001.

51. Crisanti, A., and F. Ritort. 2003. Violation of the fluctuation-dissipation theorem in glassy systems: basic notions and the numerical evidences. *J. Phys. A Math. Theor.* 36:R181–R290.